Surface heat transfer and flow properties of vortex arrays induced artificially and from centrifugal instabilities

C. S. Subramanian
Mechanical and Aerospace Engineering Department, Florida Institute of Technology, Melbourne, FL, USA

P. M. Ligrani
Department of Mechanical Engineering, University of Utah, Salt Lake City, UT, USA

M. F. Tuzzolo
Department of Mechanical Engineering, Naval Postgraduate School, Monterey, CA, USA

Fluid-flow and heat transfer properties from artificially induced vortices in a flat-plate turbulent boundary layer and naturally occurring vortices due to centrifugal instabilities in a curved-channel laminar flow are presented and compared. Pairs and arrays of vortices are artificially induced by placing half-delta wings on the plate surface. With both arrays and pairs of vortices, streamwise velocities and total pressures are high, and surface heat transfer is locally augmented in vortex downwash regions. As the spacing between the vortices increases, downwash areas span larger regions and, correspondingly, increase areas where the heat transfer is more than that for the surrounding nominally two-dimensional turbulent boundary layer. In contrast to vortices in the arrays, vortices in the pairs tend to move in the streamwise direction with significant divergence (when the common flow between pair is towards the wall) or convergence (when the common flow between pair is away from the wall). The vortices in the arrays cause maximum peak-to-peak heat transfer variations of up to 12% of local spanwise-averaged values for initial vortex spacings (assuming vortex spacing to be proportional to the vortex-generator spacing, which is measured between the mid-chord points) between 1 to 2.5 generator heights. Vortex arrays that form on concave surfaces due to centrifugal instabilities give rise to distributions of mean velocity components and surface heat transfer that are qualitatively similar to the distributions for the boundary layer with artificially generated array of vortices. Streamwise mean velocity, total pressure, and local heat transfer values are high in the vortex downwash regions and are low in the vortex upwash regions. But because the naturally developed vortices at Dean number of 100 are considerably weaker than the artificially induced vortices, they cause maximum peak-to-peak heat transfer variations of only about 6% of the local spanwise-averaged values.

Keywords: embedded vortices; centrifugal instability; vortex array; vortex spacing

Introduction

Streamwise embedded vortices in the forms of arrays and pairs are commonly found in turbomachines. Such vortices cause significant perturbations to local wall heat transfer distributions as well as to film-coolant distributions, and often lead to creation of local hot spots. Different mechanisms lead to the formation of arrays of vortices. Near concave surfaces of turbine blades, centrifugal instabilities cause faster-moving fluid to move towards the wall to displace slower-moving fluid very near the wall. Thus, fluid moves towards the wall and away from the wall. The resulting spanwise varying regions of high- and low-speed flow form into counterrotating pairs, sometimes referred to as Taylor–Görtler roll cells in boundary layers and Dean vortices in channel flows. Vortex pairs and arrays also develop from intense local pressure gradients, such as those formed at blade leading edges near end walls, or at surface protuberances.

Beginning with the measurements by Tani (1962), many researchers provide evidence of quasi-steady longitudinal

Address reprint requests to Dr. Ligrani, Department of Mechanical Engineering, MEB 3209, University of Utah, Salt Lake City, UT 84112, USA.

Received 23 July 1991; accepted 3 February 1992

vortices in turbulent boundary layers developing on concave surfaces. The presence of these vortices is indicated by the spanwise variations of measured mean quantities in an otherwise two-dimensional (2-D) mean flow. Jeans and Johnston (1982) present results from an extensive flow-visualization study in turbulent boundary layers on the concave surface of a water tunnel. They conclude that the observed boundary-layer large-scale (vortical) structures cannot be perceived as vortices because of their limited lifetimes and limited streamwise coherence. They describe vortical structures that wander in the spanwise direction, distribute randomly in space and time, and also merge, separate, appear, and disappear. In additional flow-visualization work, Barlow and Johnston (1985) identify different types of transitory motions as "large-scale outflows," "large-scale inflows," and "roll-cells." Their measurements indicate that spanwise variations of skin friction are up to 20% of spanwise-averaged values due to naturally occurring "roll cells," and up to 40% of spanwise-averaged values if vortex generators are used to fix the location of vortices. They also point out that regardless whether the vortices develop naturally or are artificially induced, they alter the turbulence structural parameters significantly compared to flat-plate turbulent boundary layers with 2-D mean flow fields. Hoffman et al. (1984) point out that there is a preferred lateral position about which the vortices wander, since the mean flow measurements on the concave surface show variations in the spanwise direction. This preferred lateral position depends upon steady nonuniformities in the oncoming flow, such as from the damping screens at the inlet of the tunnel. They also suggest that the wavelength of the spanwise variations of the mean quantities is about twice the local boundary-layer thickness, but that the spacing and the amplitude of the variations depends on the strength of initial disturbance. Simonich and Moffat (1982) present surface heat transfer rates measured on a concave wall (same facility as that of Jeans and Johnston, 1982). They indicate that the local maximum spanwise Stanton-number variation is less than 15% of the mean. Their simultaneous flow visualization and measurements near the wall show regions of quiescent fluid during the common inflow (towards the concave surface) events, suggesting that turbulence levels are suppressed near the wall. Crane and Sabzvari (1989) and Crane and Umur (1990) present results measured in unstable concave wall boundary layers. Of these two papers, the one by Crane and Umur (1990) focuses on effects of favorable pressure gradients and on the effects of precurvature boundary-layer development. Ligrani and Niver's (1988) flow-visualization pictures of a fully developed curved-channel laminar flow illustrate the development and growth of longitudinal vortices (due to centrifugal instabilities) in the Dean number range from 40 to 220. These vortices are relatively stationary at low Dean numbers in the time-averaged flow field, since they develop in a laminar rather than in a turbulent flow.

In the recent past, there have been many studies describing effects of vortices, induced artificially by using vortex generators, on the fluid-flow properties in turbulent boundary layers. Mehta and Bradshaw (1988) and Cutler and Bradshaw (1989) report the effects of vortex pairs embedded in turbulent boundary layers with the common flow between individual vortices towards the wall. Mehta et al. (1983) report the effects for both vortex pairs, with their common flow between individual vortices away from the wall and common flow between individual vortices towards the wall. Pauley and Eaton (1988) present extensive measurements of fluid-flow and heat transfer properties in a turbulent boundary layer with embedded vortex pairs and with embedded vortex arrays. They conclude that vortex pairs with common flow between them away from the wall cause the vortex centers that are initially close to the surface to move considerably away from the surface to entrain surrounding boundary-layer fluid and cause it to converge towards the plane of symmetry. With vortex pairs with common flow between them towards the wall, opposite trends are reported. The results also show that boundary-layer turbulence structure is altered significantly in the regions affected by these vortices.

Studies of heat transfer effects of embedded vortices are relatively scarce. Eibeck and Eaton (1987) show how single embedded vortices cause Stanton-number increases as great as 24% and decreases of 14%, with respect to the undisturbed values in flat-plate turbulent boundary layers. Pauley and Eaton's (1988) heat transfer measurements in a turbulent boundary-layer flow with longitudinally embedded vortices (including pairs and arrays) show that the heat transfer is augmented in vortex downwash regions and diminished in upwash regions.

The main objectives of the present study are to measure and study the development and structure of (1) vortex pairs and vortex arrays induced artificially in turbulent boundary layers for various vortex spacings, and (2) vortex arrays induced from centrifugal instabilities in a curved channel with laminar flow.

Notation

b	Vortex-generator delta wing spacing, cm
D	Channel height, cm
Nu	Nusselt number
Re	Reynolds number based on channel width
St	Stanton number with vortex
Sto	Baseline Stanton number, no vortex
T	Mean temperature
U	Mean velocity, m/s
X	Streamwise distance from boundary-layer trip, m
Y	Distance normal to the surface, cm
Z	Spanwise distance from test-surface spanwise centerline, cm

Greek symbols

δ	Undisturbed boundary-layer thickness, cm
Γ	Circulation of streamwise vorticity, m^2/s
ρ	Density, kg/m^3
ξ	Unheated starting length, m
ω	Vorticity, 1/s

Subscripts

r	Recovery condition
o	Total condition
w	Wall
x	Streamwise direction
y	Normal direction
z	Spanwise direction
∞	Freestream

The resulting flow fields are then compared to each other to determine differences and similarities between the curvature-induced vortices and artificially induced vortices. This comparison provides information on the use of artificially induced vortices for the simulation of naturally occurring vortex pairs and arrays in practical environments. These flows were chosen for comparison because a vortex structure is apparent in the time-averaged flow field for both situations. The naturally induced vortices are apparent in the time-averaged flow field, since the flow is laminar rather than turbulent. The artificially induced vortices are apparent in time-averaged measurements because their positions do not vary with time. With the artificially induced vortices, attention is additionally focused on the effects of spanwise vortex spacing. For pairs and arrays, both naturally developing and artificially induced, surface heat transfer distributions are presented along with surveys of total pressure and mean velocity components.

The following sections describe experimental apparatus and procedures, experimental uncertainties, methods to artificially induce vortex pairs and vortex arrays, and characteristics of centrifugally induced vortices. Finally, sections on experimental results and summary and conclusions follow.

Experimental apparatus and procedures

Two separate experiments are conducted to obtain data on the effects of artificially induced and curvature-induced pairs and arrays of counterrotating vortices upon the heat transfer and fluid-flow properties. In the first experiment, the vortices are induced artificially using vortex generators in a zero-pressure-gradient turbulent boundary layer in a wind tunnel. In the second experiment, two curved channels are employed to obtain data for vortices induced in laminar flow due to centrifugal instabilities. One of the channels, described by Ligrani and Niver (1988), is employed for fluid-flow measurements, and another similar channel with heated sections is employed to obtain heat transfer data.

In what follows, the wind tunnel and curved-channel facilities are described first. Then procedures employed for measuring the mean velocity in the two experiments are described. Finally, procedures employed for measuring heat transfer in the two experiments are described.

Wind tunnel and coordinate system

The wind tunnel is open-circuit, subsonic, and located in the laboratories of the Department of Mechanical Engineering of the Naval Postgraduate School. A centrifugal blower is located at the upstream end, followed by a diffuser, a header containing a honeycomb and three screens, and then a 16-to-1 contraction-ratio nozzle. The nozzle leads to the test section, which is a rectangular duct 3.05 m long and 0.61 m wide, with a topwall having adjustable height to permit changes in the streamwise pressure gradient. For the present study, a zero pressure gradient is maintained without induced vortices to within 0.18 mm of water differential pressure along the length of the test section. The air speed through the test section is 10 m/s. The freestream turbulence intensity based on the freestream velocity is just less than 0.1%. The boundary layer is tripped near the exit of the nozzle with a 1.5-mm-high strip of tape to render the boundary layer fully turbulent.

A schematic showing the test surface and coordinate system is presented in Figure 1a. With the heat transfer surface at elevated temperature, an unheated starting length of 1.10 m exists, and the direction of heat transfer is then from the wall to the air. Thermocouple row locations along the test surface are also labeled in Figure 1a. In regard to the coordinate system, Z is the spanwise coordinate measured from the test-section centerline, X is measured from the upstream edge of the boundary-layer trip, and Y is measured normal to the test surface.

Vortex generators

The vortex generators are mounted on a base plate located 0.48 m downstream of the boundary layer trip. The vortex generators consist of half-delta wings attached to a 1.6 mm-thick Lexan mounting plate. This device is attached to the wind-tunnel floor so that the generators across the span are at alternating angles of $+15°$ and $-15°$ with respect to the tunnel centerline. The height of the delta wings is 3.0 cm, and the base is 7.5 cm. The combination of three generator pairs is used to form a vortex array, as shown in Figure 1a.

Curved channel and coordinate system

As mentioned before, two curved channels are employed for the experiments. One of them, the transparent curved channel described in detail by Ligrani and Niver (1988), is used for fluid-flow measurements at a spanwise/radial plane 120° from the start of curvature. For the heat transfer measurements, a second curved channel with heat transfer surfaces is used that allows for the thermal expansion without distortion of test-section surfaces. A detailed description of the design and construction of this channel is given by Hughes (1989) and Skogerboe (1990). A schematic of the test surface is shown in Figure 1b.

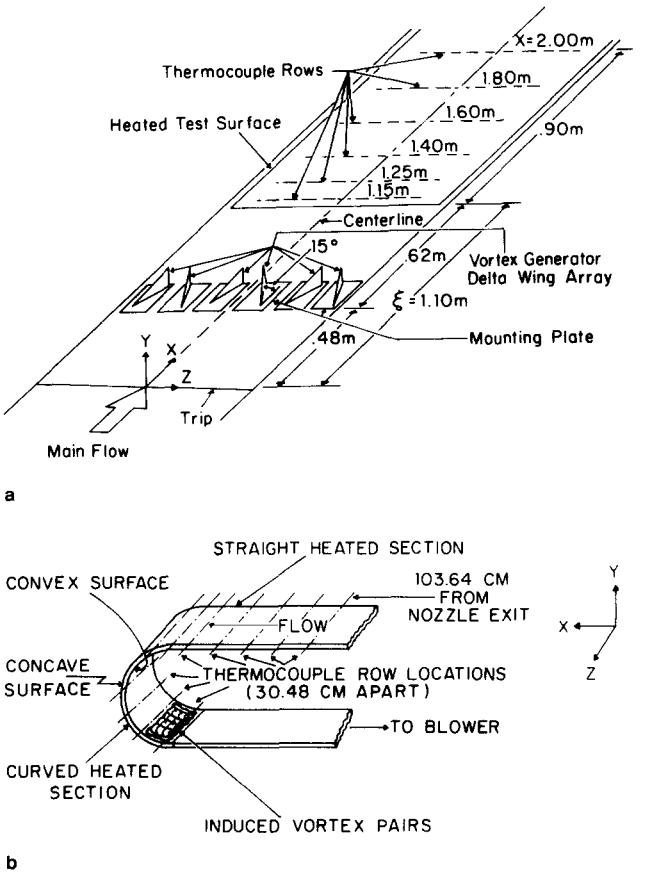

Figure 1 Coordinate system and schematic for (a) wind-tunnel test section, and (b) curved-channel test section

A brief summary of constructional features common to both channels is presented here. Each channel has an interior rectangular cross section of 1.27 cm by 50.96 cm, giving an aspect ratio of 40 to 1. The rectangular duct inlet section contains an aluminium honeycomb and three wire screens all placed normal to the flow direction. As the air exits the 25.4-cm-by-50.96-cm duct section, it enters a 20-to-1 contraction-ratio nozzle. After exiting the nozzle, air first enters a straight section, 2.44 m long, 1.27 cm high, and 50.96 cm wide. The straight section allows hydrodynamically fully developed channel flow to develop before the flow enters the curved section for Dean numbers less than 640. The Dean number is equal to $\mathrm{Re}(D/r)^{0.5}$, where r is the surface radius of curvature of the convex surface of the curved channel. After the straight section, the fluid then enters the 180° curved-channel section with a convex surface radius of 59.69 cm and a concave surface radius of 60.96 cm. Upon exiting the curved section, the air then enters the second straight section with a length of 2.44 m. As the flow leaves the second straight portion, it passes through four screens, a honeycomb, a diffuser with a total angle of 3°, and finally into a plenum chamber. An ICG industries-type 10-P blower, capable of producing 10.2 cm of water vacuum at 4.82 m^3/min volumetric flow rate, is used to depressurize a second plenum to pressures just below atmospheric pressure. With this system, flow rates can be varied to produce Dean numbers from 10 to 435. Flow rates are measured by means of a pressure drop across an orifice plate placed in piping between the two plenums. The channel coordinate X is in the streamwise direction measured from the inlet of the straight section, coordinate Z is in the spanwise direction and measured from the centerline, and coordinate Y is normal to channel surfaces measured from the concave surface.

Mean velocity measurements

In the wind-tunnel surveys, three mean velocity components are measured using a five-hole pressure probe with a conical tip of diameter 6.35 mm, manufactured by United Sensors Corporation. Celesco transducers and Carrier Demodulators are used to sense pressures when connected to probe output ports. To obtain surveys of streamwise velocity and secondary-flow vectors, the five-hole probe is traversed, in increments of 5.08 mm, over spanwise/ normal planes (800 probe locations) using an automated 2-D traversing system that may also be placed at different streamwise locations. The mean streamwise vorticity contours are then calculated from the secondary-flow vectors.

Using the channel described by Ligrani and Niver (1988), total pressure and the three mean velocity components are measured with a miniature five-hole probe of tip diameter 1.22 mm (Ligrani et al., 1989b). The probe is traversed in a spanwise radial plane located at 120° from the start of curvature. The probe traversing is done over a channel cross-sectional area that is 5.08 cm in the spanwise direction and 1.02 cm in the radial direction in increments of 1.27 mm. Following Ligrani et al. (1989a), corrections are made to account for spatial resolution and downwash velocity effects during data reduction.

The experimental setup and procedures employed here are validated by performing some baseline checks. Baseline data for the open circuit, subsonic wind tunnel where the basic boundary-layer flow is turbulent are composed of mean velocity components and vorticity results with single embedded vortices. These results show good consistency with the results of Shabaka et al. (1985) and Westphal et al. (1987). Channel-flow mean velocity components and vorticity results for the centrifugally induced vortex arrays show agreement with the results of Baun (1988).

Heat transfer measurements

In the wind tunnel, the heat transfer surface is designed to provide a constant heat flux over its area. The surface next to the airstream is stainless steel foil painted flat black. Immediately beneath this is a liner containing 126 thermocouples in six rows, which is just above a Marchi Assoc. wire-wound heater rated at 120 volts and 1500 watts. The thermocouples are used to measure temperatures along the surface of the test plate. Two other thermocouples are used to measure the ambient and the freestream temperatures. Located below the heater are several layers of insulating materials including Lexan sheets, foam insulation, styrofoam, and balsa wood. Surface-temperature levels and convective heat transfer rates are controlled by adjusting power into the heater using a Standard Electric Co. type 3000B variac. To determine the heat loss by conduction, an energy balance was performed. Radiation losses from the top of the test surface were analytically estimated. The thermal contact resistance between thermocouples and the foil top surface was estimated on the basis of outputs of the thermocouples and measurements from calibrated liquid crystals on the surface of the foil. This difference was then correlated as a function of heat flux through the foil. After determination of the convective heat flux to the air, local heat transfer coefficients are determined based on the difference between the wall temperature and freestream recovery temperature. These are then used for calculation of local Stanton numbers. More details on the heat transfer surface and heat transfer measurements are given by Ligrani et al. (1991) and by Tuzzolo (1989).

The heat transfer surfaces in the curved channels are similar in construction to the one employed in the wind tunnel. Etched foil heaters, manufactured by the Electrofilm Corporation, are installed on each of the two lexan surfaces of the channel. These heaters provide a constant heat flux to both the concave and convex surfaces, all at the same heat rates, to produce uniform boundary conditions at the straight inlet portion and curved portion of the channel. The dimensions of each heater are 38.1 cm by 1.524 m, and the power capacity is 2000 watts. Heaters are placed so that the leading edges of the heaters are 0.884 m from the channel inlet and the trailing edges of the heaters end approximately 38.1 cm from the completion of channel curvature. Each heater is powered by a Superior Electric type 136B variac. With each variac, the voltage to a heater may be adjusted between 0 and 115 volts, and the current may be adjusted from 0 to 10 amps. Power inputs to each heater are determined by measuring voltage drops across 50 mv, 10 amp shunt resistors to determine heater current, as well as the voltage drop across each heater.

Two hundred Copper-Constantan thermocouples manufactured by Omega Engineering Corp. are placed on the channel surfaces to allow some spatial resolution of surface-temperature distributions. In the present study, results are presented for the curved section only. One hundred and seventy thermocouples are located on the curved section walls in five spanwise rows of 17 per row. Each row of thermocouples is spaced 30.48 cm part in the X direction. Of the 17 thermocouples in each spanwise row, two are located near the edges of the channel, with the remaining 15 placed over a spanwise extent of approximately 5.08 cm over the central span of the channel. These thermocouples allow determination of local Nusselt numbers in the presence of two pairs of Dean vortices (because approximate spanwise spacing for each pair is about two channel heights), from which spanwise-averaged Nusselt

numbers are determined. Four additional thermocouples are used to measure ambient temperatures around the outside of the channel, mixed-mean temperature at the air inlet, and mixed-mean temperature at the channel outlet. To minimize conducted heat loss to the surroundings and to maximize the amount of convective heat transfer into the channel, the outside of the entire heated portion of the channel is insulated with black foam insulation manufactured by the Halstead Company. For this study, an additional row of 2.5 cm insulation is attached along all edges of the heated channel to further minimize conduction from heated channel walls. Conduction heat loss magnitudes are estimated based on energy balances around the channel. Radiation is neglected, and the thermal contact resistance between thermocouples and convective surfaces is estimated using the same procedures employed for the wind-tunnel tests. After the local convective heat flux is determined, local heat transfer coefficients and Nusselt numbers are determined based on the difference between the local wall temperature and local mixed-mean temperature.

For the heat transfer surfaces on the channel and on the wind tunnel, thermocouple voltages are acquisitioned and recorded using HP3497A low-speed Data Acquisition Control Units and HP3498A Extenders. The data processing is done using Hewlett Packard/series 9000 model 310 computers.

Baseline heat transfer measurements for the wind tunnel consist of spanwise-averaged Stanton numbers when there is no vortex in the flow. These show good agreement with the correlation from Kays and Crawford (1980), with a maximum deviation of 5% for the situation in which an unheated starting length exists followed by a constant heat-flux boundary condition. Further checks on the measurement apparatus and procedures are made by measuring spatial variations of Stanton numbers along the test surface with single embedded vortices. These data are also consistent with other results in the literature (Ligrani et al., 1989c, 1991; Elbeck and Eaton, 1987).

Two types of baseline tests qualify measurement procedures and apparatus employed for the curved heated channel. First, the spanwise-averaged Nusselt number values determined for zero buoyancy effects from measurements on both surfaces of the initial straight section range from 8.11 to 8.45 when the laminar flow is thermally fully developed at Dean numbers of 100 and 125. This result is in excellent agreement with the correlation given by Kays and Crawford (1980), who indicate that the average Nusselt number is 8.24 for fully developed laminar flow between two infinite parallel plates with constant heat-flux boundary conditions. Second, the mixed-mean temperatures measured at the exit of the curved section for different Dean numbers closely match values determined from an energy balance. Further qualification is provided by measurements in the thermal entry length of the channel, which show expected behavior, and by the fact that measurements on the two different surfaces match at each streamwise location.

Experimental uncertainties

Uncertainty estimates are based upon 95% confidence levels and are determined using procedures described by Kline and McClintock (1953) and Moffat (1982). Typical nominal values of freestream recovery temperature and wall temperature are 18.0°C and 40°C with respective uncertainties of 0.13°C and 0.21°C. The freestream density, freestream velocity, and specific heat uncertainties are 0.009 kg/m^3 (1.23 kg/m^3), 0.06 m/s (10.0 m/s), and 1 J/kgK (1006 J/kgK), where typical nominal values are given in parenthesis. The uncertainty estimates for the secondary-flow velocity components, U_y and U_z, are 0.09 m/s (1.0 m/s). For convective heat transfer, heat transfer coefficient, and heat transfer area, 10.5 W (270 W), 1.03 W/m^2 K (24.2 W/m^{2}K), and 0.0065 m^2 (0.0558 m^2), respectively, are typical uncertainties. The uncertainties of St and St/Sto are 0.000086 (0.00196) and 0.058 (1.05), respectively. The uncertainties of Dean number and Nusselt number are 4.4 (150.0) and 0.37 (6.00), respectively.

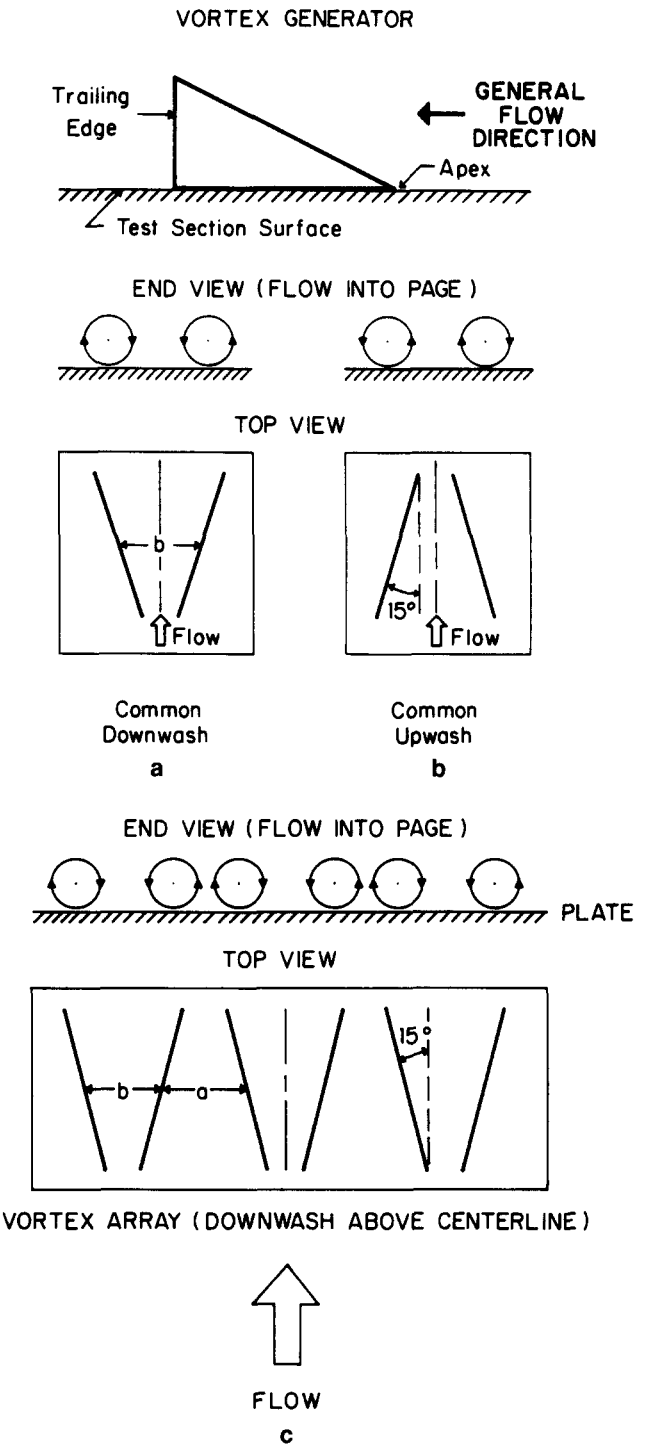

Figure 2 Vortex-generator arrangements and orientations for (a) vortex pair with common downwash between the two individual vortices, (b) vortex pair with common upwash between the two individual vortices, and (c) vortex array with downwash region located above the test-surface spanwise centerline

Methods to artificially induce vortex pairs and vortex arrays

A vortex pair is created when two vortex generators are positioned together as depicted in Figures 2a and 2b. As mentioned earlier, each vortex is generated using a half-delta wing mounted on the wind-tunnel test surface at an angle of attack to the oncoming flow. A common downwash between the two vortices in a pair is created when the apex of each vortex generator is closer to the centerline than the trailing edge, as shown in Figure 2a. The opposite effect of a common upwash between the two vortices in a pair is created when the apex of each vortex generator is farther away from the tunnel centerline than the trailing edge, as shown in Figure 2b. The spanwise spacing between vortices is varied by changing the parameter b (see Figures 2a and 2b), the spanwise distance between midchord of vortex generators. This is done in our study to provide information on practical environments where vortex spacings in pairs can vary widely. For the vortex pairs, the b values used are 2.54, 3.81, 5.08, 6.35, and 7.62 cm.

Spanwise arrays of pairs of counterrotating vortices are produced using vortex-generator arrangements like the one depicted in Figure 2c. With this arrangement, three pairs of vortices are produced from six individual vortex generators such that the vortices in the middle pair of the array have a common downwash along the tunnel centerline. With a second arrangement, the vortices in the middle pair of the array have a common upwash along the tunnel centerline. Within each array, an individual vortex pair consists of two adjacent vortices with a common upwash between them. With both arrangements of vortex generators used to produce arrays, the spacing between the two vortices within each pair is maintained constant by keeping the spacing parameter a (shown in Figure 2c) constant at 6.35 cm. When the vortices in the middle pair have a common upwash along the tunnel centerline, the geometry parameter b (shown in Figure 2c) is also maintained at 6.35 cm, which is connected to the spanwise extents of downwash regions and to the spanwise spacing between vortex pairs. When the vortices in the middle pair have a common downwash along the tunnel centerline, geometry parameter b is set equal to 3.81, 5.08, and 6.35 cm to produce situations with different spacings between vortex pairs. The spanwise extents of resulting downwash regions then also vary accordingly.

Arrays of vortex pairs induced by centrifugal instabilities

When subjected to concave curvature, flows near surfaces eventually develop pairs of counterrotating vortices as a consequence of centrifugal instabilities. These initially manifest themselves by imposing larger forces on the faster-moving fluid near the central portions of channel flows, or alternatively on the freestream flow just outside of the boundary layers. This faster-moving fluid then moves towards the concave surface to displace slower-moving fluid near the wall, which is initially pushed in the spanwise direction and then away from the wall. Thus, a flow with high streamwise speeds that is moving towards the wall is adjacent to a flow with lower streamwise velocities that is moving away from the wall. The resulting variations of high- and low-speed fluid across the span of the flow then develop into pairs of counterrotating vortices. As mentioned earlier, these vortices are called Dean vortex pairs in channels and Görtler vortices in boundary layers.

A discussion of characteristics of vortices induced artificially and of vortices that develop from centrifugal instabilities is presented in the next section. This is followed by a discussion of the relation between the vortex characteristics and local heat transfer distributions.

Experimental results

In this section, data are first presented from the wind-tunnel experiments for the artificially induced vortex pairs and the artificially induced vortex arrays. For all the measurements, the freestream speed is about 10 m/s. This is followed by discussion of the centrifugally induced vortex arrays that form in the curved channels.

Characteristics of artificially induced vortex pairs

Some characteristics of the vortex pairs produced using vortex-generator arrangements are illustrated by results presented in Figures 3a, 3b, and 3c for b values of 2.54 cm, 5.08 cm, and 7.62 cm, respectively. These show secondary-flow vectors measured in a spanwise/normal plane at $X = 1.48$ when the common flow between the two vortices in a pair is towards the surface (downwash regions). Streamwise velocity contours, to be discussed shortly, are also included in these figures. In these views, the streamwise flow direction is into the plane of the page, and approximately circular clockwise and counterclockwise secondary-flow vectors are apparent, which evidence individual vortices.

Corresponding magnitudes of the maximum streamwise vorticity, circulation of streamwise vortices, and locations of vortex centers are given in Table 1. Maximum vorticity values are given for both vortices in each pair, where local streamwise vorticity is given by $(\partial U_z/\partial Y - \partial U_y/\partial Z)$, which is determined using finite-difference equations applied to secondary-flow vector distributions. Table 1 shows that vorticity values for individual vortices within each pair are about the same. In addition, peak vorticity and vortex circulation generally increase as the spacing between vortex pairs (spacing parameter b) increases, until $b \geqslant 5.08$ cm when values for the two largest spacings ($b = 5.08$ cm and 7.62 cm) are about the same. Circulation magnitudes are calculated by integrating streamwise vorticity with respect to spanwise/normal plane area. To minimize the influences of background noise, the integration is performed assuming that all vorticity values less than a threshold of 76.0 (1/s) are equal to zero. The same numerical threshold is employed for all measurement points. This value is chosen because it is equal to 10% of the peak vorticity level in a single vortex produced by a single generator with the same geometry employed presently (Ligrani et al., 1989c, 1990, 1991). Circulation magnitudes are given in Table 1 only for the clockwise vortex (as viewed looking downstream) because the net circulation of a pair is usually about zero. The Ycenter and Zcenter values in Table 1 locate the center of the clockwise vortex, determined at the location of peak vorticity. Vortex-center locations from the wall (Ycenter) do not change with b, even though Zcenter decreases proportionately.

As mentioned earlier, Figures 3a, 3b, and 3c show secondary-flow vectors superimposed on longitudinal mean-velocity contours. The secondary-flow vectors from the vortices result in regions of upwash where the secondary-flow vectors move away from the surface, and in regions of downwash where the secondary-flow vectors move towards the surface. In Figure 3a, the downwash region extends from $Z = -5.0$ cm to $Z = 5.0$ cm, and upwash regions are present for $Z \geqslant 6.0$ cm and $Z \leqslant -6.0$ cm. Distributions of streamwise velocity are illustrated by the contour lines, which show that the local boundary-layer thickness is increased in upwash regions. This

Table 1 Characteristics of vortices arranged in pairs for different spacings between vortices at $X = 1.48$ m

Vortex-generator spacing b (cm)	Maximum clockwise streamwise vorticity (1/s)	Maximum counter-clockwise streamwise vorticity (1/s)	Circulation for the clockwise streamwise vortex (m^2/s)	Ycenter for the clockwise streamwise vortex (cm)	Zcenter for the clockwise streamwise vortex (cm)
2.54	287	342	0.065	2.48	−5.59
5.08	666	638	0.096	2.48	−7.11
7.62	677	not measured	0.096	2.48	−8.13

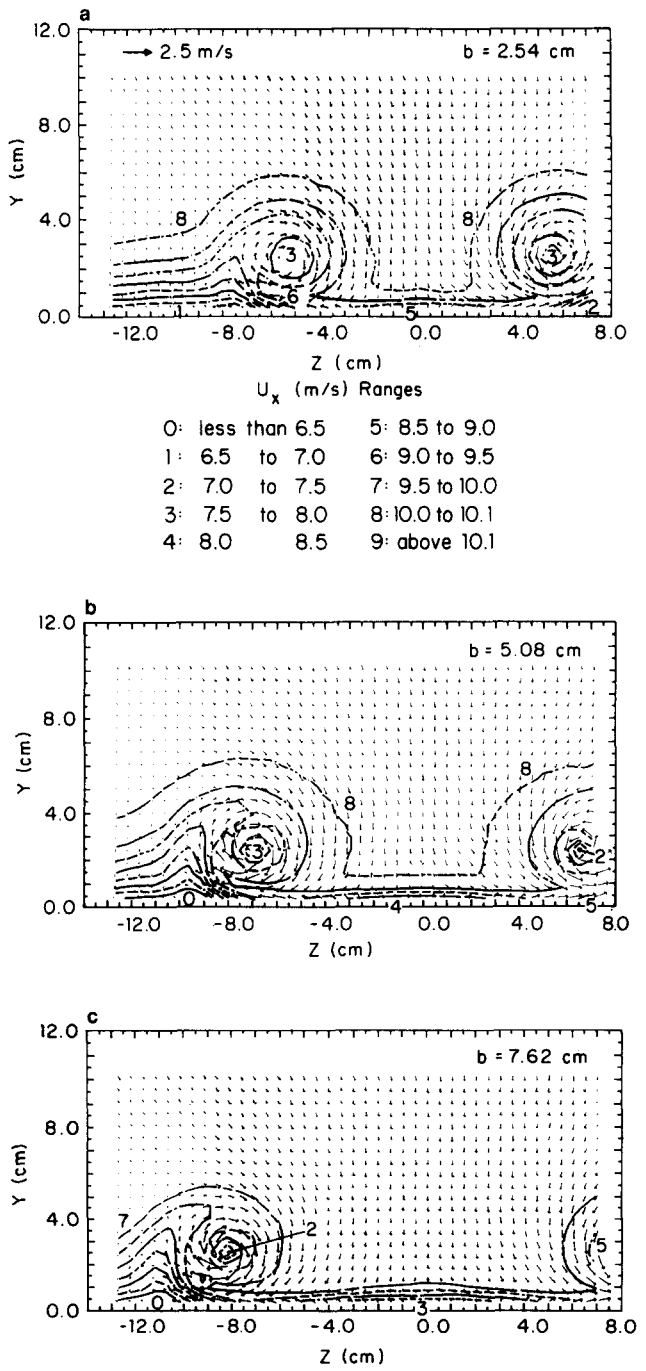

Figure 3 Streamwise velocity contours and secondary-flow vectors in a boundary layer at $X = 1.48$ m with an artificially induced embedded vortex pair. (a) $b = 2.54$ cm, (b) $b = 5.08$ cm, and (c) $b = 7.62$ cm

is because low-momentum fluid is convected away from the wall by the secondary flows. In downwash regions, high-velocity freestream fluid is brought close to the wall by the secondary flows. Consequently, the boundary layer is locally thinned. Downwash regions separate the two vortices within each pair, such that the vortex on the left is clockwise rotating and the vortex on the right is counterclockwise rotating (when viewed looking downstream). Further examination of Figures 3a, 3b, and 3c reveals that downwash regions cover larger spanwise portions of the test surface as b increases. Even for the largest vortex-generator separation in the spanwise direction, $b = 7.62$ cm (about 2.5 generator heights), the boundary layer is still considerably thin (boundary-layer thickness, δ, is 1.2 cm) in the downwash region as compared to the undisturbed local boundary-layer thickness ($\delta \sim 2.8$ cm). This result is consistent with that of Pauley and Eaton (1988), who noted that a boundary-layer thinning effect persists even at vortex-generator spacing of 7 vortex-generator heights.

Streamwise mean-velocity deficits are also apparent within the vortices shown in Figures 3a, 3b, and 3c. These are caused by wakes from vortex generators, which are rolled into vortex cores by secondary-flow vectors. Approximate locations of vortex centers are thus indicated by the presence of local velocity deficits. Strong secondary-flow vectors are apparent everywhere around vortex centers and vortex core regions, especially beneath the vortex centers near the wall.

Characteristics of artificially induced arrays of vortex pairs

The situation in which an array of vortices is produced such that the middle pair has a common downwash along at the tunnel centerline is illustrated by results presented in Figure 4a ($a = 6.35$ cm, $b = 5.08$ cm) and in Figure 4b ($a = 6.35$ cm, $b = 6.35$ cm). These figures present secondary-flow vectors measured in a spanwise/normal plane at $X = 1.48$ m. Also included in these figures are streamwise velocity contours, which will be discussed shortly. Downwash regions at the spanwise centerline of the test section ($Z = 0.0$ cm) are apparent in both Figures 4a and 4b. When compared to the vortex pair results in Figures 3a, 3b, and 3c, the results in these two figures show qualitatively different distributions of streamwise mean velocity and secondary-flow vectors. This is primarily because upwash regions in the arrays are compressed into smaller areas (in spanwise/normal planes) and intensified because of the close proximity in the spanwise direction of the individual vortices within each pair. In such vortex arrays, upwash regions are thus considered to separate the two vortices within each vortex pair.

Characteristics of individual vortices in the array are given in Table 2. These results include magnitudes of maximum vorticity, vortex circulation, and locations of the vortex centers, and are given for the vortex pairs located between 0.0 cm and −10.0 cm in Figures 4a and 4b. In reference to these pairs in each of these figures, the clockwise vortex is located on the

Table 2 Characteristics of vortices arranged in arrays for different spacings between vortex pairs at $X = 1.48$ m

Vortex-generator spacing b (cm)	Maximum clockwise streamwise vorticity (1/s)	Maximum counter-clockwise streamwise vorticity (1/s)	Circulation for the clockwise streamwise vortex (m^2/s)	Ycenter for the clockwise streamwise vortex (cm)	Zcenter for the clockwise streamwise vortex (cm)
5.08	578	559	0.14	5.5	−4.0
6.35	486	582	0.12	6.54	−3.0

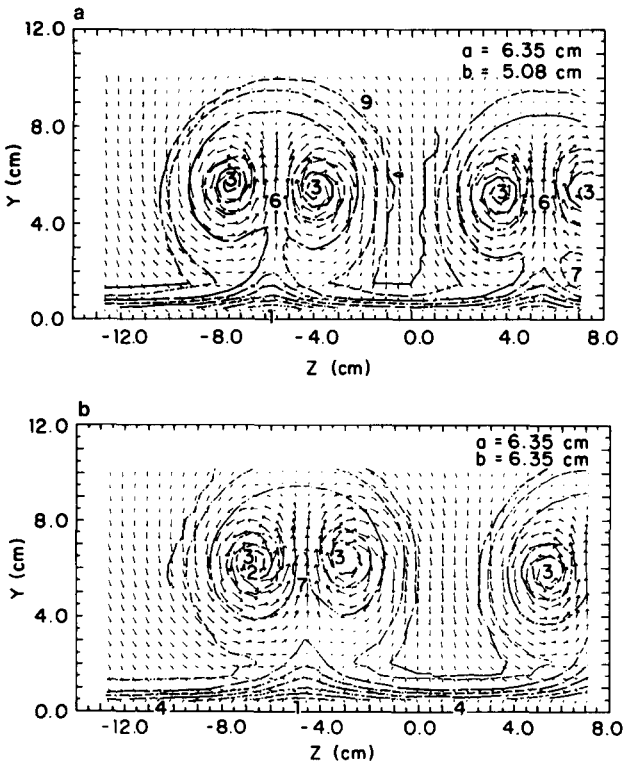

Figure 4 Streamwise velocity contours and secondary-flow vectors in a boundary layer at $x = 1.48$ m with an artificially induced embedded vortex array; $a = 6.35$ cm. (a) $b = 5.08$ cm, and (b) $b = 6.35$ cm. Velocity contour levels are given in Figure 3

right and the counterclockwise vortex is located on the left (as viewed looking downstream). Table 2 shows that maximum vorticity magnitudes and magnitudes of circulation generally increase somewhat as the spacing between the vortex pairs decreases (spacing parameter b). For the $b = 6.35$ cm data, the vortex center for the clockwise vortex is at Ycenter = 6.54 cm and Zcenter = −3.0 cm, and for the $b = 5.08$ cm data, Ycenter = 5.5 cm and Zcenter = −4.0 cm. On comparing the characteristics of the individual vortices in the array to the characteristics of individual vortices in the pairs, several important differences are evident. Firstly, for the same b values, the peak vorticity magnitudes are less and the circulation values are greater for the vortices in array than for the vortices in the pairs. Secondly, vortex-center distances from the wall change significantly and spanwise distances between vortex centers change very little with b in the array, whereas the opposite is true with vortex pairs. In the latter case, centers of vortices in pairs change significantly in the spanwise direction, even though distance from the test surface does not change with b. This is because vortices in the paired configurations diverge (for common downwash pairs) and converge (for common upwash pairs) with streamwise development. In contrast, the vortices in the arrays tend to move in the streamwise direction without as much convergence or divergence. Any convergence or divergence that is present results because upwash regions become compacted and intensified in the arrays, which causes adjacent vortices to move somewhat away from downwash regions and away from the wall. This motion away from the wall also results because of pressure distributions in the flow that are produced because of the secondary flows that convect high-velocity/high-pressure freestream flow near the walls beneath individual vortices (Figures 4a and 4b). Such behavior then leads to further rearrangement of individual vortices as they are convected downstream, as well as to local increases in boundary-layer thickness, indicated by contours of the streamwise mean velocity in Figures 4a and 4b.

These streamwise velocity contours show mushroom-shaped patterns, where the portions appearing as mushroom stems are locations of low-momentum fluid that is convected away from the wall within upwash regions. In downwash regions, high-velocity/high-pressure freestream fluid is not only brought near the wall by secondary flows but is also arranged so that it is located between vortex pairs. As a result, the fluid containing individual vortices is pushed towards the low-pressure upwash regions. Thus, the vortices with common upwash between them tend to move closer together with streamwise development because of the differences in pressure on either side of individual vortices. As mentioned earlier, this produces upwash regions that are much more compacted and intensified compared to downwash regions.

Mean longitudinal vorticity contours for the vortex array with $a = 6.35$ cm and $b = 6.35$ cm are shown in Figure 5. Consistent with the nature of secondary-flow vectors in Figure 4b, the pair of contours on the left of the test-section centerline

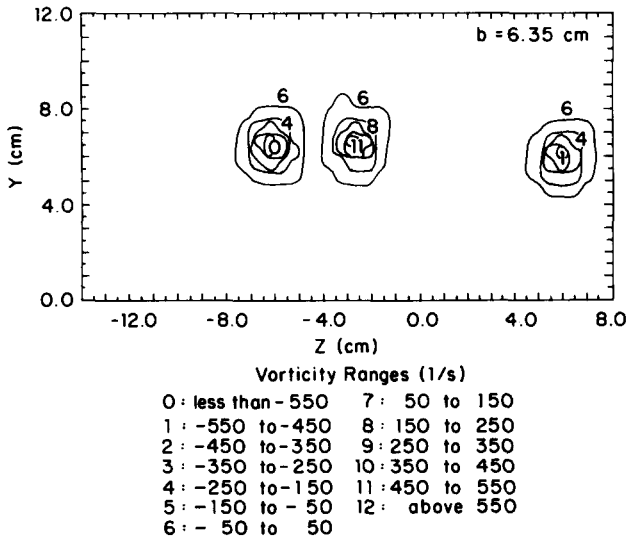

Figure 5 Streamwise vorticity contours in a boundary layer with an embedded vortex array at $x = 1.48$ m, $a = 6.35$ cm, and $b = 6.35$ cm

represent a clockwise (or positive) vortex and a counterclockwise (or negative) vortex within one vortex pair. These vorticity contours also illustrate vorticity levels that are nearly circular in shape. In addition, magnitudes within the positive vortex are about equal to absolute-value magnitudes in the negative vortex for the entire range of vorticity levels measured.

Characteristics of vortex pair arrays induced from centrifugal instabilities

Some time-averaged characteristics of centrifugally induced vortices measured in a curved channel with mild curvature and a 40-to-1 aspect ratio are elucidated in Figures 6a and 6b. These data were obtained 120° from the start of curvature at a Dean number of 100 (Baun 1988; Fields 1990). The first of these figures shows variations of the streamwise mean velocity across a portion of the spanwise/radial plane. Associated streamwise vorticity distributions are shown in the subsequent figure. The concave surface of the channel is located on the bottom of each plot in Figures 6a and 6b so that $Y/D = 0$ corresponds to the concave surface and $Y/D = 1$ corresponds to the convex surface. The bulk flow direction is then into the plane of the page.

Vortices formed in the curved channel at these experimental conditions have several time-averaged features in common with the arrays of artificially induced vortices described earlier. As with artificially induced vortices, regions of low velocity and high velocity exist that correspond, respectively, to upwash and downwash regions (with respect to the concave surface) between individual vortices. Such variations are present because secondary flows from the vortices within the array rearrange portions of the flow field with different streamwise velocity magnitudes. Downwash regions of the vortices convect high-momentum streamwise fluid from near the channel center towards the region near the concave wall, whereas vortex upwash regions result in the convection of low-momentum streamwise fluid from near the concave surface towards the region near the center of the channel. As for the artificially induced vortex arrays, spanwise extents of upwash regions are smaller than the downwash regions, again as a result of higher-pressure fluid existing on the downwash sides of individual vortices and lower-pressure fluid existing on the upwash sides of individual vortices. Upwash regions are identified in Figure 6a at locations of streamwise velocity deficits that are present near the concave surface at Z/D spanwise locations of 5.1, 6.0, and 7.2. Each deficit thus exists between the two vortices within each vortex pair. Downwash regions (with respect to the concave wall) are apparent at Z/D of 4.5, 5.6, 6.5, and 7.7 at locations where streamwise mean velocities are high near the concave wall. Average spacing between the vortex pairs, estimated from the distance between upwash regions, is about one channel width.

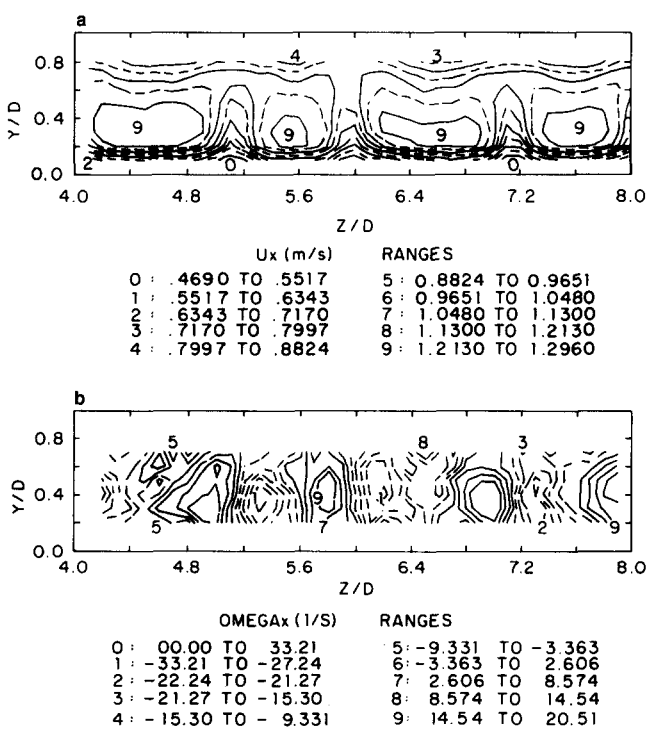

Figure 6 (a) Streamwise velocity contours, (b) streamwise vorticity contours in curved-channel flow at Dean number of 100, as measured in a spanwise/radial plane located 120° from start of curvature

Figure 6b shows streamwise vorticity contours also at a Dean number of 100, which illustrate how individual vortex pairs are spread across the measurement plane with respect to upwash regions. These contours are obtained from secondary-flow vectors using the same procedures described for the artificially induced vortices. Here, continuous-line contours indicate regions of positive vorticity, and broken-line contours show regions of negative vorticity. About three distinct pairs of Dean vortices are noticeable in the figure. Peak absolute values of vorticity at this Dean number range from 28 1/s to 33 1/s, depending upon which vortex across the measurement plane is considered. Corresponding magnitudes of circulation range from 4.0 to 7.5 m^2/s (Fields 1990). Such vortices increase in strength as the Dean number increases, and at a particular Dean number, with streamwise development. Values of peak vorticity reach 70–85 1/s at Dean numbers from 200 to 240. However, even these values are significantly smaller than values for the artificially induced vortices presented in Table 1.

Differences in the channel vortex arrays and the wind-tunnel vortex arrays exist mostly because the flow in the curved channel is bounded, whereas the freestream flow in the wind tunnel is, of course, not constrained by a solid boundary. Because of this, vortices in the channel may not move away from the concave surface and expand as they do when they are present in boundary layers developing along the test surface of the wind tunnel. In addition, the continual application of centrifugal instabilities causes curved-bounded-channel vortices to become stronger as they develop downstream along the curved channel. The artificially induced vortices, on the other hand, become weaker and more diffuse as they convect downstream (Ligrani and Schwartz 1990). These levels of diffusion are significantly higher than ones in the centrifugally induced vortices because much higher levels of turbulence are present within the artificially induced vortices. In regard to streamwise velocity magnitudes for the two situations, the maximum-to-minimum streamwise velocity ratio is about 2.8 for centrifugally induced vortices, whereas the ratio is only about 1.6 for the arrays of artificially induced vortices.

Surface heat transfer beneath artificially induced vortex pairs

Normalized surface heat transfer distributions beneath pairs of artificially induced vortices are presented in Figures 7 and 8. These data are given in terms of local Stanton number ratios St/Sto, where St represents the local Stanton number when embedded vortices are present, and Sto represents the local Stanton number baseline values when no embedded vortices are present. St/Sto values greater than or less than 1.0 then

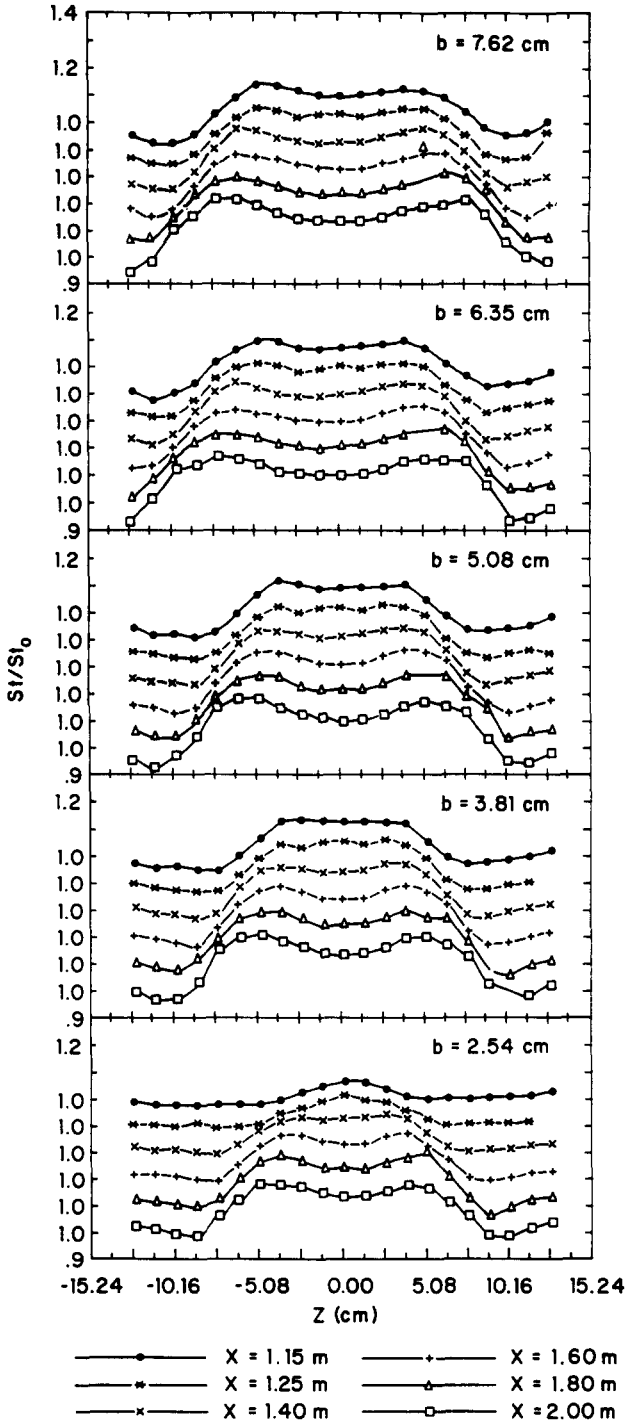

Figure 7 Local Stanton-number ratio distributions as measured beneath vortex pairs with downwash regions between the two individual vortices for b values ranging from 2.54 cm to 7.62 cm

correspond to regions where local heat transfer coefficients are higher or lower than the values that would exist in a turbulent boundary layer with a 2-D mean flow field that developed naturally in the same location. Data in Figures 7 and 8 are given for different spacings between vortex pairs corresponding to b values from 2.54 cm to 7.62 cm, where b is illustrated in Figure 2 as the spanwise spacing between the delta wings used to generate the vortices. For each vortex pair spacing, St/Sto distributions across the span of the wind-tunnel test surface are presented for X-coordinate locations of 1.15, 1.25, 1.40, 1.60, 1.80, and 2.00 m. To prevent plotting data points on top of one another and to clarify the streamwise development, the St/Sto scale for each set of data is displaced relative to the scales corresponding to other sets of data.

In Figure 7, St/Sto ratio distributions are presented for the situation in which the area between the two vortices within each pair (near the test-section centerline) is a downwash region. In this downwash region, St/Sto ratio magnitudes are greater than 1.0 because of secondary flows that convect high-velocity freestream fluid near the test surface, resulting in a turbulent boundary layer that is locally thinned. The two

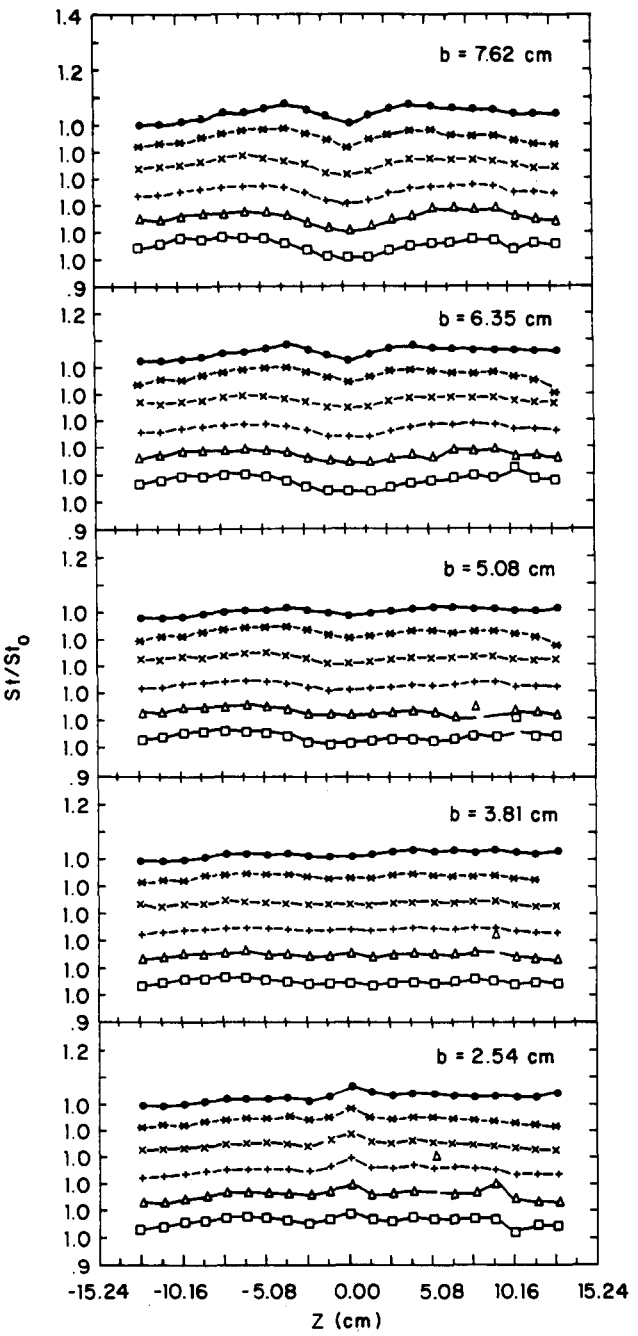

Figure 8 Local Stanton-number ratio distributions as measured beneath vortex pairs with upwash regions between the two individual vortices for b values ranging from 2.54 cm to 7.62 cm

vortices that bound this flow diverge from each other as they convect downstream, which also causes the three-dimensional (3-D) boundary layer between them to diverge. As this happens, both spanwise extents of high St/Sto and peak values of St/Sto increase with streamwise distance (note that absolute values of St decrease with X, but that is offset by greater decreases of Sto with X). For example, for $b = 2.54$ cm, at $X = 1.15$ m, St/Sto values are greater than 1.0 for $-5.0\text{ cm} \leqslant Z \leqslant 5.0\text{ cm}$, and the peak magnitude of St/Sto is 1.07. At $X = 2.00$ m, St/Sto values are greater than 1.0 for $-8.0\text{ cm} \leqslant Z \leqslant 8.0\text{ cm}$, and the peak magnitude of St/Sto is about 1.18. In comparison, the data of Pauley and Eaton (1988) show a peak St/Sto value in the downwash region between two diverging vortices (within a pair) of about 1.23, which may be due to their stronger vortices. Their results are also different from ones from the present investigation because their peak St/Sto values do not change significantly with streamwise development.

The results in Figure 7 also provide information on the effects of spacing between the two vortices within each pair. Maxima St/Sto in downwash regions generally increase with spacing between these two vortices. Spacings associated with larger values of b also correspond to wider downwash regions in the lateral direction, as well as to larger areas along the test surface where St/Sto > 1.0. Considering results for $b = 2.54$ cm and $X = 1.15$ m shows that St/Sto values are greater than 1.0 for $-5.0\text{ cm} < Z < 5.0\text{ cm}$. With $b = 7.62$ cm, the region where St/Sto > 1.0 is increased, extending from $Z = -7.0$ cm to $Z = 7.0$ cm. The results for both these b values for $X = 1.40$ m are consistent with the velocity survey results in Figure 3a for $b = 2.54$ cm and in Figure 3c for $b = 7.62$ cm. In both cases, the velocity results are given for $X = 1.48$ m, and the approximate boundaries of augmented St/Sto regions correspond to locations beneath the centers of the vortices. As mentioned earlier, these centers are identified in Figures 3a and 3c by local deficits of the streamwise mean velocity, which are located approximately 2.48 cm away from the wall.

Figure 8 shows St/Sto distributions when the flow between the two vortices within a pair (near the wind-tunnel centerline, $Z = 0.0$ cm) is an upwash region. Here, the secondary-flow vectors in between the vortex pairs are directed approximately opposite to the ones shown in Figure 3a, 3b, and 3c. With this arrangement, secondary flows moving away from the surface result in local increases in the boundary-layer thickness and larger accumulations of low-velocity fluid near the wall. The upwash region is also a region where the local boundary layer converges as the two vortices on either side of this region converge towards each other with streamwise development. The mechanism for this behavior has been mentioned earlier, but in another context, i.e., diverging boundary layers and downwash regions. Here, the converging vortices result because of low pressures in the fluid between the two vortices and high pressures on the other sides of each individual vortex. These pressure differences result because of flow rearrangement by vortex secondary flows.

In the study of Pauley and Eaton (1988), St/Sto values deviate from 1.0 by only small amounts between vortex pairs with a common upwash between them compared to vortex pairs with a common downwash between them. Similar behavior is evident from results in Figure 8, especially for b values of 2.54 cm and 3.81 cm. Thus, the combination of low streamwise velocities near the wall and increased boundary-layer thicknesses produce St/Sto perturbations that are less significant than those resulting from thinned boundary layers and that are high near wall velocities (Figure 7). Since the centers of the converging vortices tend to be located away from the wall as they are convected downstream, such behavior supports the idea that heat transfer rates are altered only if the vortices are located near surfaces. Pauley and Eaton (1988) further suggest that significant perturbations to local heat transfer distributions depend upon the strength of the interactions between the two vortices. For $b = 5.08$, 6.35, and 7.62 cm, the present results in Figure 8 show a slightly larger St/Sto decreases from 1.0 as more intense upwash regions provide slightly greater perturbations, especially near the spanwise centerline of the test surface. For these situations, St/Sto values different from 1.0 are evident from $Z = -2.5$ cm to $Z = 2.5$ cm, and little change with streamwise development or spanwise vortex spacing is apparent.

Surface heat transfer beneath artificially induced arrays of vortex pairs

St/Sto distributions measured beneath artificially induced vortex arrays are presented in Figures 9 and 10. In the first of these figures, results are given for the same situation illustrated by Figure 2c, wherein the vortex array is arranged so that a downwash region is present over the spanwise centerline of the test surface. In this figure, parameters a and b are labeled. By altering b, spacings between vortex pairs are changed across the span of the test surface, where an individual pair comprises two vortices with a common upwash between them. Results in Figure 9 are presented for b values of 3.81 cm, 5.08 cm, and 6.35 cm, with a equal to 6.35 cm for all three situations. Results in Figure 10 are given for the situation in which the vortex array is arranged so that an upwash region is present over the spanwise centerline of the test surface. To produce this flow,

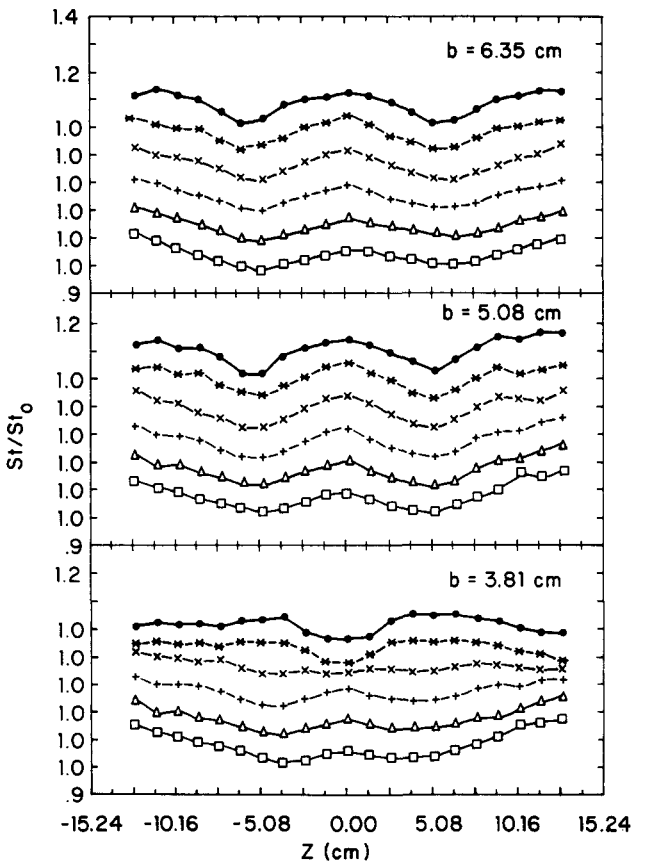

Figure 9 Local Stanton-number ratio distributions as measured beneath arrays of vortex pairs arranged so that a downwash region is present above the spanwise centerline of the test surface; $a = 6.35$ cm, $b = 3.81$ cm, 5.08 cm, and 6.35 cm

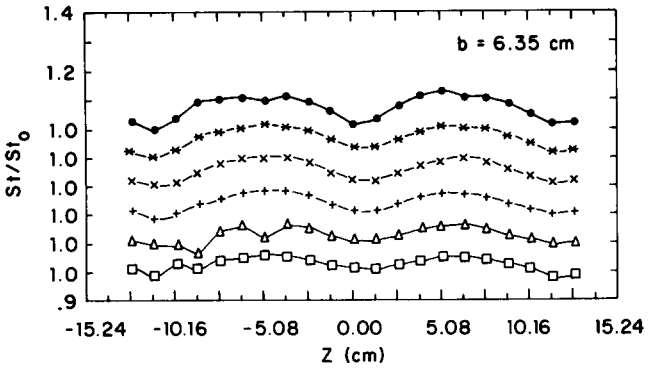

Figure 10 Local Stanton-number ratio distributions as measured beneath arrays of vortex pairs arranged so that an upwash region is present above the spanwise centerline of the test surface; $a = 6.35$ cm, $b = 6.35$ cm

the vortex generators in Figure 2c are arranged with angles of opposite sign to the ones shown (i.e., changed from $+15°$ to $-15°$), and with parameters a and b both equal to 6.35 cm.

In Figures 9 and 10, St/Sto values are given across the span of the test surface for six different streamwise locations for each vortex array arrangement investigated. For all four arrangements, St/Sto values are generally greater than 1.0 beneath downwash regions and less than 1.0 beneath upwash regions. This is particularly evident if results in Figure 9 for $b = 5.08$ cm and $b = 6.35$ cm are compared to velocity survey results for the same conditions in Figures 4a and 4b, respectively. Considering St/Sto data for all four vortex-array configurations, local St/Sto augmentations for arrays are generally somewhat less than the local augmentations that result for artificially induced vortex pairs. Maximum and minimum St/Sto values from the arrays are 1.15 and 0.97, respectively, which also provides some evidence that downwash regions cause stronger perturbations to local heat transfer coefficients than upwash regions. These St/Sto variations are comparable to ones observed by Simonich and Moffat (1982), who measured surface heat transfer rates on a concave wall with turbulent water flow passing over it. They found local maximum Stanton number values to generally be within 15% of spanwise-averaged Stanton number values. Their flow-visualization and near wall measurements additionally show regions of quiescent fluid within downwash regions, which, according to the authors, suggests that the turbulence levels and turbulent heat transport are suppressed within these regions near the wall.

Further examination of Figures 9 and 10 reveals that the spanwise extents of downwash regions where St/Sto > 1.0 become somewhat larger with X. Such variations result because upwash regions become compacted and intensified as arrays are convected downstream, which causes adjacent *individual vortices* to move away from downwash regions and away from the wall. Velocity survey data in Figures 4a and 4b illustrate such behavior, and also provide evidence that vortex *pairs* within an array tend to move in the streamwise direction without the convergence or divergence that occurs when only one vortex pair develops along the test surface. This is consistent with results in Figures 9 and 10, since the spanwise locations of local maxima and local minima corresponding to downwash and upwash regions show almost no changes with X. In Figure 9, spanwise extents of St/Sto > 1 regions associated with vortex downwashes increase slightly as b is changed from 3.81 cm to 5.08 cm. However, little change in the spanwise extents of associated downwash regions results as b is changed from 5.08 cm to 6.35 cm.

The results in Figure 10 for $a = 6.35$ cm and $b = 6.35$ cm are comparable to those in Figure 9 for the same a and b, except that they are displaced in the spanwise direction by a distance corresponding to the spanwise extent of a single vortex. In Figure 10, results evidence an upwash region near $Z = 0.0$ cm, and St/Sto values are less than 1.0 for $-2.0 \text{ cm} \leqslant Z \leqslant 2.0$ cm at $X = 2.00$ m. Neighboring downwash regions in the array correspond to St/Sto values greater than 1.0.

Surface heat transfer beneath vortex pair arrays induced from centrifugal instabilities

Results that illustrate normalized surface heat transfer distributions beneath vortex pair arrays induced from centrifugal instabilities are presented in Figure 11. These were measured along the concave surface of the curved channel described earlier at four different streamwise locations corresponding to X/D of 202.8, 251.0, 275.2, and 299.4, where X is measured from the channel inlet and D is the channel height. The channel is arranged so that the first 2.44 m from the inlet is straight, and thus, mild curvature begins at $X/D = 192.0$. Nusselt numbers presented in Figure 11 as a function of Z/D are based on the hydraulic diameter (which equals two channel heights). These results are given for a Dean number of 98.6, which corresponds to a bulk mean flow velocity of about 0.8 m/s. The measurements of local Nusselt numbers spanned a spanwise distance Z of 3.8 cm, or a Z/D of about 3.0 such that surface variations beneath two to three pairs of vortices are resolved. Additional discussion of the thermal behavior and characteristics of these Dean vortices is given by Skogerboe (1990), who determined local Nusselt numbers along concave and convex surfaces in the same channel employed in the present study at Dean numbers ranging from 50 to 200.

The first features of Figure 11 discussed are the variations of Nu values as dependent upon X/D. For this, one must consider spanwise averages at each X/D of the locally varying data in Figure 11. Initially, at $X/D = 202.8$ (or 10.8 channel heights from the start of curvature), the spanwise-averaged Nusselt number is just above 6.0. At larger downstream distances from the start of curvature (59.0 to 107.4 channel heights, or $X/D = 251.0$ to 299.4), spanwise-averaged Nusselt numbers increase and then remain somewhat constant with X/D as the influences of the centrifugal instabilities are believed

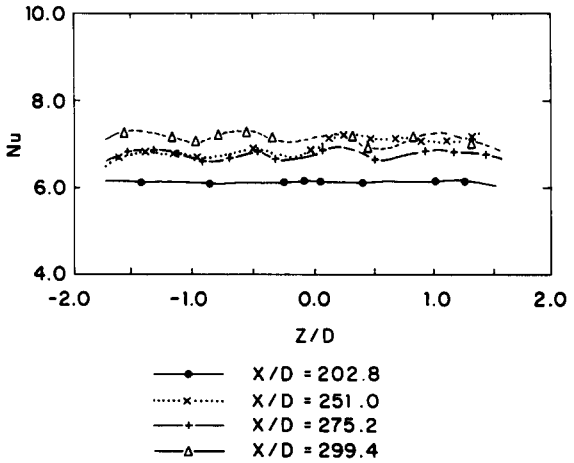

Figure 11 Local Nusselt numbers measured along the concave surface of the curved channel at a Dean number of 98.6 as a function of Z/D for X/D ranging from 202.8 to 299.4

to become more pronounced. Some of the variations shown are also believed to be due to the influences of buoyancy on the pressure-driven flow in the channel.

The imposition of the centrifugal instabilities also coincides with important spanwise variations of local Nu values as a result of the formation of Dean vortex pairs. Upwash and downwash regions (with respect to the concave surface) within and on the sides of individual vortices result in variations of the streamwise mean velocity and total pressure at different locations across the span of the channel. Near the concave surface, these variations are then closely correlated with spatial variations of local Nusselt numbers. As with the artificially induced vortex arrays, local heat transfer coefficients are augmented beneath downwash regions and diminished beneath upwash regions. However, the maximum peak-to-peak spanwise variation in the heat transfer coefficient in Figure 11 is only about 6% of the spanwise-averaged value. In contrast, with the artificially induced vortex array described earlier, the maximum peak-to-peak spanwise variation in the heat transfer coefficient is 12% of the spanwise averaged value at any particular streamwise location. This difference is most likely because the vortices in the channel are weaker than the artificially induced vortices. For example, the peak vorticity levels in the channel at the experimental conditions of Figure 11 are in the range from 28 1/s to 33 1/s, which is an order of magnitude smaller than the peak vorticity levels present for the artificially induced vortices. Vortices become stronger in the curved channel at shorter streamwise distances as the Dean number increases, and these stronger vortices produce larger perturbations to local heat transfer coefficient distributions. Thus, some of the differences between the artificially induced and centrifugally induced vortices are certainly due to the different velocity levels present in the two environments. However, the centrifugally induced vortices would be expected to be somewhat weaker than the artificially induced vortices even if equivalent velocity levels were present. In addition, the more intense channel vortices become wavy and wander in space (Ligrani and Niver, 1988; Ligrani et al., 1992), which would produce time-averaged results that are somewhat smeared and reduced in magnitude compared to a situation in which the vortices are stationary in time and space (i.e., the artificially induced vortices).

Summary and conclusions

Characteristics of artificially induced vortices and vortices initiated by centrifugal instabilities are presented and compared. Also examined are the effects of changing some of the properties of the artificially induced vortices, including spanwise spacing between the two vortices contained within single pairs of counterrotating vortices, and the spanwise spacings of vortex pairs contained within an array of vortices. For all situations, the vortices are composed of boundary-layer fluid and develop near surfaces. The artificially induced arrays and pairs of vortices were produced using half-delta wings mounted on the test surface of an open-circuit, subsonic wind tunnel. The boundary-layer flow in this facility was turbulent, with Reynolds numbers based on streamwise distance varying from 8.0×10^5 to 1.4×10^6. The natural vortices developing from centrifugal instabilities formed in a curved rectangular channel with a 40-to-1 aspect ratio where the flow is laminar at a Dean number near 100. These two types of vortices were chosen for comparison because they both produce identifiable features in the measured time-averaged flow fields. For the study, measurements are made of streamwise mean-velocity distributions, distributions of secondary-flow vectors, and distributions of the streamwise mean vorticity, as well as variations of normalized heat transfer coefficients along surfaces. For the wind-tunnel surveys of the artificially induced vortices, the heat transfer coefficients are expressed in terms of Stanton numbers, whereas for the channel surveys, these heat transfer coefficients are given in terms of Nusselt numbers.

The centrifugal instability induced vortices have a number of time-averaged features similar to ones measured in the artificially induced arrays of vortices. For both situations, regions of low velocity and high velocity exist that correspond, respectively, to upwash and downwash secondary-flow regions (with respect to the concave surface in the channel, and with respect to the test surface in the wind tunnel). In the channel, downwash regions of the vortices convect high-momentum streamwise fluid from near the channel center towards the region near the concave wall, whereas vortex upwash regions result in the convection of low-momentum streamwise fluid from near the concave surface towards the region near the center of the channel. Near the concave surface of the channel, the resulting variations of streamwise velocity are closely correlated with spatial variations of local Nusselt numbers. At 59.0 to 107.4 channel heights from the start of curvature, spanwise-averaged Nusselt numbers increase and then remain somewhat constant with streamwise distance as the influences of the centrifugal instabilities are believed to become more pronounced. The imposition of these centrifugal instabilities also coincides with augmented local heat transfer coefficients beneath downwash regions and diminished local heat transfer coefficients beneath upwash regions. These local variations in the spanwise direction are qualitatively similar to ones present beneath the upwash and downwash regions of the artificially induced vortex arrays.

For both types of arrays, the vortex pairs tend to move in the streamwise direction without strong convergence or divergence, and the spanwise extents of upwash regions are smaller than the downwash regions as a result of high-pressure fluid existing on the downwash sides of individual vortices and lower-pressure fluid existing on the upwash sides of individual vortices. These pressure distributions are produced because of the secondary flows that convect high-velocity/high-pressure freestream flow near the walls beneath individual vortices as well as between vortex pairs. As a result, the fluid containing individual vortices is pushed towards the low-pressure upwash regions, which are compacted and intensified compared to downwash regions.

Differences between the artificially induced vortex array and the centrifugally induced array exist mostly because the flow in the curved channel is bounded, whereas the freestream flow in the wind tunnel is, of course, not constrained by a solid boundary. Because of this, vortices in the channel may not move away from the concave surface and expand as much as they do when they are present in boundary layers developing along the test surface of the wind tunnel. In addition, the continual application of centrifugal instabilities causes curved-bounded-channel vortices to become stronger as they develop downstream along the curved channel. The artificially induced vortices, on the other hand, become weaker and more diffuse as they convect downstream. These levels of diffusion are significantly higher than ones in the centrifugally induced vortices because much higher levels of turbulence are present within the artificially induced vortices. The artificially induced vortex arrays produce maximum peak-to-peak heat transfer coefficient variations of about 12% of spanwise-averaged values, whereas the maximum peak-to-peak spanwise variations of heat transfer coefficients is only about 6% of local spanwise-averaged values beneath the centrifugally induced vortex arrays. This is mostly because the naturally developing

vortices are considerably weaker (peak vorticity values are 28–33 l/s) than the artificially induced vortices (peak vorticity values are 290–700 l/s).

In contrast to vortices in the arrays, artificially induced vortices in pairs tend to move in the streamwise direction with significant divergence (when the common flow between the two vortices is towards the wall) or convergence (when the common flow between the two vortices is away from the wall). For the former situation, the divergence of the two vortices also causes the 3-D boundary layer between them to diverge. As this happens, both spanwise extents of high St/Sto and peak values of St/Sto increase with streamwise distance for constant initial vortex spanwise spacing. As the initial spanwise spacing between the vortices in a pair increases, downwash areas span larger distances, giving larger regions of high heat transfer. For the latter situation in which the flow between the two vortices in a pair is an upwash region, the local boundary layer between them also converges with streamwise development. This converging region contains locally lower heat transfer coefficients compared to ones that would exist beneath a nominal 2-D turbulent boundary layer at the same locations.

Acknowledgments

The work presented in this report was sponsored by two different organizations: (1) the Office of the Naval Research in conjunction with the Naval Postgraduate School Direct Research Program (Dr. Spiro Lekoudis and Dr. Edwin Rood of ONR were program monitors), and (2) the Propulsion Directorate, U.S. Army Aviation Research and Technology Activity-AVSCOM through NASA-Defense Purchase Request C-30030-P (Mr. Kaz Civinskas of AVSCOM was program monitor). Some of the facilities used were purchased using funds from the Naval Postgraduate School Foundation Research Program. All of the work presented was done at the Naval Postgraduate School, Monterey, CA, USA.

References

Barlow, R. S. and Johnston, J. P. 1985. Structure of turbulent boundary layers on a concave surface. Rept. MD-47, Thermosciences Division, Department of Mechanical Engineering, Stanford University, Stanford, CA

Baun, L. R. 1988. The development and structural characteristics of Dean vortices in a curved rectangular channel with 40 to 1 aspect ratio. M.E. Thesis, Naval Postgraduate School, Monterey, CA

Crane, R. I. and Sabzvari, J. 1989. Heat transfer visualization and measurement in unstable concave wall boundary layers. *ASME Trans.-J. Turbomachinery*, **111**, 51–56

Crane, R. I. and Umur, H. 1990. Concave-wall laminar heat transfer and Görtler vortex structure: effects of pre-curvature boundary layer and favorable pressure gradients. ASME paper 90-GT-94

Cutler, A. D. and Bradshaw, P. 1989. Vortex/boundary layer interactions. AIAA Paper AIAA-89-0083

Eibeck, P. A. and Eaton, J. K. 1987. Heat transfer effects of a longitudinal vortex embedded in a turbulent boundary layer. *ASME Trans.-J. Heat Transfer*, **104**, 355–362

Fields, W. A. 1990. Study of the effects of centrifugal instabilities on flow in a 40 to 1 aspect ratio rectangular curved channels for Dean numbers from 160 to fully turbulent conditions. M.E. Thesis, Department of Mechanical Engineering, Naval Postgraduate School, Monterey, CA

Hoffman, P. H., Muck, K. C., and Bradshaw, P. 1985. The effect of concave surface curvature on turbulent boundary layers. *J. Fluid Mech.*, **161**, 371–403

Hughes, R. E. 1989. Development, qualification and measurements in two curved channels with 40 to 1 aspect ratio. M.S. Thesis, Department of Mechanical Engineering, Naval Postgraduate School, Monterey, CA

Jeans, A. H. and Johnston, J. P. 1982. The effects of streamwise concave curvature on turbulent boundary layer structure. Rept. MD-40, Thermosciences Division, Department of Mechanical Engineering, Stanford University, Stanford, CA

Kays, W. M. and Crawford, M. E. 1980. *Convective Heat and Mass Transfer*, second ed, McGraw-Hill, New York

Kline, S. J. and McClintock, F. A. 1953. Describing uncertainties in single-sample experiments. *Mech. Eng.*

Ligrani, P. M., Finlay, W. H., Fields, W. A., Fuqua, S. J., and Subramanian, C. S. 1992. Features of wavy vortices in a curved channel from experimental and numerical studies. *Phys. Fluids A*, **4**(4), 695–709

Ligrani, P. M. and Niver, R. D. 1988. Flow visualization of Dean vortices in a curved channel with 40 to 1 aspect ratio. *Phys. Fluids*, **31**, 3605–3617

Ligrani, P. M., Ortiz, A., Joseph, S. L., and Evans, D. L. 1989c. Effects of embedded vortices on film-cooled turbulent boundary layers. *ASME Trans.-J. Turbomachinery*, **111** (1), 71–77

Ligrani, P. M. and Schwartz, G. E. 1990. Control of embedded longitudinal vortices using a wall jet. *Int. J. Heat Fluid Flow*, **11** (4), 274–283

Ligrani, P. M., Singer, B. A., and Baun, L. R. 1989a. Spatial resolution and downwash velocity corrections for multiple-hole pressure probes in complex flows. *Exp. Fluids*, **7** (6), 424–426

Ligrani, P. M., Singer, B. A., and Baun, L. R. 1989b. Miniature five-hole pressure probe for measurement of mean velocity components in low speed flows. *J. Phys. E-Sci. Instruments*, **22** (10), 868–876

Ligrani, P. M., Subramanian, C. S., Craig, D. W., and Kaisuwan, P. 1991. Effects of vortices with different circulations on heat transfer and injectant downstream of a single film-cooling hole in a turbulent boundary layer. *ASME Trans.-J. Turbomachinery*, **113** (3), 433–441

Mehta, R. D. and Bradshaw, P. 1988. Longitudinal vortices imbedded in turbulent boundary layers. Part II. Vortex pair with "common flow" upwards. *J. Fluid Mech.*, **188**, 529–546

Mehta, R. D., Shabaka, I. M. M. A., Shibl, A., and Bradshaw, P. 1983. Longitudinal vortices embedded in turbulent boundary layers. AIAA Paper AIAA-83-0378

Moffat, R. J. 1982. Contributions to the theory of single-sample uncertainty analysis. *ASME Trans.-J. Fluids Eng.*, **104**, 250–260

Pauley, W. R. and Eaton, J. 1988. The fluid dynamics and heat transfer effects of streamwise vortices embedded in a turbulent boundary layer. Rept.-51, Thermosciences Division, Department of Mechanical Engineering, Stanford University, Stanford, CA

Shabaka, I. M. M. A., Mehta, R. D., and Bradshaw, P. 1985. Longitudinal vortices imbedded in turbulent boundary layers. Part 1. Single vortex. *J. Fluid Mech.*, **155**, 37–57

Simonich, J. C. and Moffat, R. J. 1982. Local measurements of turbulent boundary layer heat transfer on a concave surface using liquid crystals. Rept. HMT-35, Thermosciences Division, Department of Mechanical Engineering, Stanford University, Stanford, CA

Skogerboe, P. E. 1990. Local and spatially averaged heat transfer distributions in a curved channel with 40 to 1 aspect ratio for Dean numbers from 50 to 200. M.S. Thesis, Department of Mechanical Engineering, Naval Postgraduate School, Monterey, CA

Tani, I. 1962. Production of longitudinal vortices in the boundary layer along a concave wall. *J. Geophys. Res.*, **67**, 3075

Tuzzolo, M. F. 1989. Study of vortex arrays induced artificially and from centrifugal instabilities. M.E. Thesis, Department of Mechanical Engineering, Naval Postgraduate School, Monterey, CA

Westphal, R. V., Pauley, W. R., and Eaton, J. K. 1987. Interaction between a vortex and a turbulent boundary layer, Part I: Mean flow evolution and turbulence properties. NASA Technical Memorandum 88361.